Materials Science and Engineering B 177 (2012) 1120–1125

Contents lists available at SciVerse ScienceDirect

Materials Science and Engineering B

journal homepage: www.elsevier.com/locate/mseb

Short communication

Effect of carbon content on the microstructure and properties of W–Si–C–N coatings fabricated by magnetron sputtering

Junfeng Yang, Yan Jiang, Zhigang Yuan, Xianping Wang, Qianfeng Fang*

Key Laboratory of Materials Physics, Institute of Solid State Physics, Chinese Academy of Sciences, Hefei 230031, People's Republic of China

ARTICLE INFO

Article history:
Received 5 February 2012
Received in revised form 24 April 2012
Accepted 28 May 2012
Available online 17 June 2012

Keywords:
Hardness measurements
W–Si–C–N
Residual stresses
Wear

ABSTRACT

A series of W–Si–C (4–5 at.%)–N nanocomposite coatings with different C contents have been deposited on Si wafer substrates by reactive magnetron sputtering of W–Si–C composite target in $Ar + N_2$ mixed atmosphere. Microstructure characteristics and mechanical properties of W–Si–C–N coatings were investigated in this paper. Results exhibited that W–Si–C–N coatings possess nanocomposite microstructure where nano-crystallites W_2(C, N) embedded in amorphous matrix of Si_3N_4/CNx/C. As the C content increased, the hardness and Youngs' modulus of the W–Si–C–N coatings first increased and then decreased, reaching the maximum value of approximate 36 GPa and 382 GPa, respectively, for coatings containing 11.1 at.% C. All the coatings are in compressive stress state, ranging from 0.8 to 2.0 GPa. In addition, friction coefficient of the W–Si–C–N coatings considerably decreased with the increase of C content.

1. Introduction

Among ternary transition metal–silicon–nitrogen coating systems, Ti–Si–N hard coating has been most widely researched. Results showed that this kind of coatings have nanocomposite structure consisted of crystalline titanium nitride and amorphous silicon nitride, where amorphous silicon nitride phase as an excellent barrier for a penetration of oxygen to the substrate surface through the coating can improve oxidation resistance of this coating [1–4]. In addition, Ti–Si–N coating shows super or ultra hardness (40–105 GPa) and also better stability at elevated temperature (>1000 °C) [5–7]. However, its friction coefficient is higher (0.6–0.8), which restrict them to be widely used in the field of cutting [8–10]. Although the quaternary Ti–Si–C–N coating, formed by incorporation of C into ternary Ti–Si–N coating, exhibits lower friction coefficient of 0.5 than that of Ti–Si–N coating [11], it is still too high to apply in high speed or dry cutting field.

In comparison to Ti–Si–N coating, W–Si–N coating is a less studied system. Previous researches showed that sputtered W–Si–N coatings possess high hardness, better thermochemical stability and fracture toughness [12,13]. Czyzniewski [14] found that W–C coatings containing approximately 90 at.% of carbon have friction coefficient lower than 0.1. Thus, quaternary W–Si–C–N coating is expected to have high hardness and low friction coefficient. However, up to now, W–Si–C–N coatings were still barely investigated. Here, we report the synthesis and characterization of W–Si–C–N coatings grown by closed field unbalance reactive magnetron sputtering. Evolution of microstructure and mechanical properties of the coatings was investigated as a function of carbon content.

2. Experimental procedure

2.1. Deposition

W–Si–C–N films were deposited onto silicon wafer (10 mm in thickness) substrates by reactive direct current magnetron sputtering techniques from a tungsten target enchased with Si (99.999%) and C (99.999%) insets, the target is 60 mm in diameter and 5 mm in thickness. The C content in the films can be adjusted by varying the area of the C inset. High purity N_2 and Ar were used as the reactive and sputtering gas, respectively.

Si wafer substrates were cleaned according to the procedure described in literature [15]. Substrate holder was electrically grounded, no bias voltage was applied. The distance from target to substrate was fixed at 60 mm.

Prior to deposition, the vacuum chamber was pumped down to a base pressure of 2×10^{-3} Pa, then the substrates were heated up to 450 °C, followed by the introduction of high-purity argon gas with the mass flow rate of 30 sccm controlled by mass flow controller (MFC). Pre-sputtering was carried out, with argon gas pressure of 1 Pa, sputtering power of 120 W and sputtering time of 20 min, in order to clean and equilibrate the target surface. After pre-sputtering, nitrogen gas was introduced into vacuum chamber;

* Corresponding author.
E-mail address: qffang@issp.ac.cn (Q. Fang).

0921-5107/$ – see front matter © 2012 Elsevier B.V. All rights reserved.
http://dx.doi.org/10.1016/j.mseb.2012.05.021

Table 1
Elemental composition of W–Si–C–N coatings as determined by XPS.

Coating number	Elemental composition (at.%)			
	W	Si	C	N
1	56.2	4.2	0	39.6
2	53.9	4.0	4.0	38.1
3	50.6	4.6	7.2	37.6
4	48.5	4.3	11.1	36.1
5	44.2	4.9	14.7	36.2
6	41.3	4.1	17.8	36.8
7	39.1	5.1	21.3	34.5

Nitrogen flow rate was set to 40 sccm; The work pressure and sputtering power were kept constant at 0.7 Pa and 100 W, respectively.

The carbon content in the coating was changed in the range of C/(C + W + Si + N) = 0–21.3 at.% as determined by the X-ray photoelectron spectroscopy (XPS) in order to investigate the effect of C content on the properties of W–Si–C–N coatings.

2.2. Characterization

Thickness of the W–Si–C–N coatings was characterized by a field emission scanning electron microscope (FESEM, Sirion 200, FEI). The crystallographic phases of the coatings were characterized by glancing-angle X-ray diffraction (XRD, Philips X'pert PRO MPD) with incident angle of 1°, in the scanning range from 30° to 90° with a step of 0.06°, using monochromatized Cu Kα radiation (λ = 1.5406 Å) operating at 40 kV and 40 mA.

An X-ray photoelectron spectroscopy (XPS, Japan, Axis ultradld) with Al (mono) Kα radiation at a pass energy of 160 eV was used to characterize the chemical bonding state and elemental composition of the deposited films. Before commencing the measurement, Ar+ ion beam with an energy of 3 keV was used to etch the sample surface for 15 min to remove contaminants. The elemental composition of the coatings determined by XPS was listed in Table 1. Microstructural information on the films was obtained by a field emission transmission electron microscope (JEOL, JEM-2010) operating at 200 kV. Raman spectroscopy with a 488 nm Ar+ laser was employed to evaluate the carbon atomic bonds of coatings.

Hardness (*H*) of the coatings was measured with a nanoindenter (MTS NANO Indenter® G200) in a continuous stiffness measurement (CSM) mode at room temperature. The residual stress of W–Si–C–N coatings was measured using stress tester [J&L Tech, JLCST022] based on Stoney formula.

The tribological behavior of W–Si–C–N coatings was measured on the CETR UMT-2 micro–macro tribometer in reciprocating mode under ambient atmospheric condition (20 ± 5 °C and 50 ± 5% RH). Bearing steel (AISI 52100) ball with diameter of 3 mm was chosen as the counterpart. All the tests were performed at a sliding velocity of 0.1 m s^{-1}; the normal load was 2 N; the sliding stroke was 2 mm. Wear volume measurements were carried out using Wyko NT1100 3D optical surface profiler.

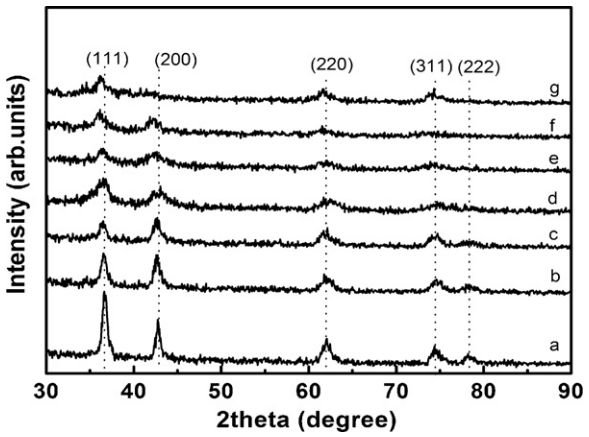

Fig. 2. XRD patterns of W–Si–C–N coatings with different carbon content: (a) 0 at.%, (b) 4.0 at.% C, (c) 7.2 at.% C, (d) 11.1 at.% C, (e) 14.7 at.% C, (f) 17.8 at.% C, (g) 21.3 at.% C.

3. Results and conclusion

Fig. 1(a, b) presents surface morphology and corresponding cross-section image of W–Si–C (11.1 at.%)–N coating, for comparison, the cross-section image of Mo–W–N coatings with coarse columnar structure [15] was presented in Fig. 1c. W–Si–C (11.1 at.%)–N coating possesses a very smooth and dense surface consisted of granular nano-particles with size of about 80 nm and a closely packed columnar cross-section with thickness of about 1 μm was observed, which was largely different from that in Fig. 1c due to the formation of nanocomposite structure in W–Si–C–N coatings.

3.1. Crystal structure and chemical bond state

Fig. 2 shows the X-ray diffraction patterns of the W–Si–C–N coating with different C content. It can be seen that all the coatings show face centered cubic (fcc) structure being confirmed by the appearance of five diffraction peaks from the (1 1 1), (2 0 0), (2 2 0),

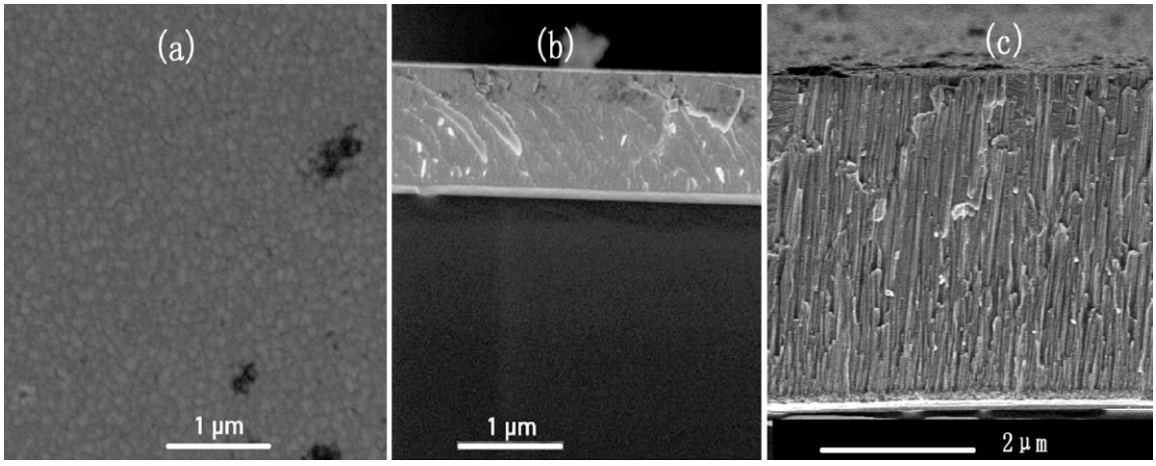

Fig. 1. (a, b) SEM images of surface and cross-section of W–Si–C (11.1 at.%)–N coating, (c) cross-section image of Mo–W–N coatings.

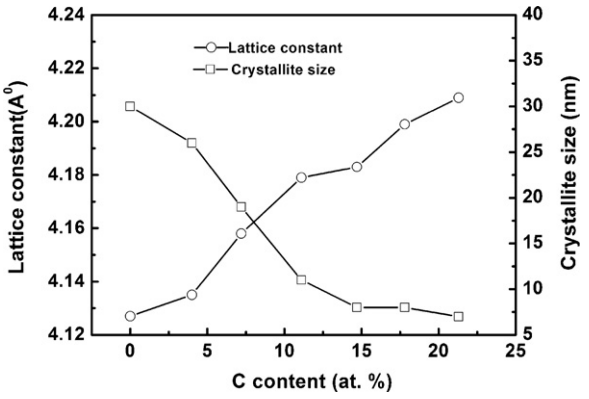

Fig. 3. Lattice constant and crystallite size of W–Si–C–N coatings with different carbon concentration.

(3 1 1), (2 2 2) crystal planes, respectively. For W–Si–N coating without addition of carbon, there was a strong (1 1 1) preferential orientation. As carbon was incorporated into W–Si–N coatings, the growth of (1 1 1) preferred orientations was restrained. This indicates that adding C into W–Si–N coatings somewhat change the texture of W–Si–N coatings. Other diffraction peaks corresponding to crystalline phases such as WSi_2, C, CNx, Si_3N_4 did not appear. This result postulated that C existed in the form of substitution for N atoms in W_2N crystal or in amorphous phases of silicon carbide, CNx or C. In addition, a peak broadening phenomenon was observed with the increase of carbon content in the W–Si–C–N coatings, which indicated the decrease of crystallite size. As shown in Fig. 3, the crystallite size decreases gradually from 30 nm to 7 nm as the C content increases from 0 at.% to 21.3 at.%. Similar XRD peak broadening phenomenon with C addition has been reported for Ti–C–N [16] and Ti–Si–C–N [17,18]. In contrast to decrease of crystallite size, the lattice parameter of W–Si–C–N coatings continually increased with increasing C content (Fig. 3), corresponding to the phenomena that the diffraction peak of W–Si–C–N coating shifted to lower angle with the increase of C content as shown in Fig. 2. This suggests the formation of W–C–N solid solution where C atoms partially replaced N atoms in the fcc W_2N crystal lattice or the coexistence of fcc W_2N and fcc β-WC_{1-x} phase because of (1) atomic radius of C atom is bigger than that of N atom, and (2) The lattice parameter of β-WC_{1-x} (a = 4.235, from JCPDS No. 20-1316) is bigger than that of W_2N (a = 4.126, from JCPDS No. 25-1257). Furthermore, taking into account the affinity of $H(W_2N) = -17$ kcal/mol, $H(Si_3N_4) = -178$ kcal/mol, $H(WC) = -8.4$ kcal/mol [19], the following order can be expected for the phase formation in W–Si–C–N coating: $Si_3N_4 \rightarrow W_2N \rightarrow WC$. The WC phase can form only when the nitrogen partial pressure is insufficient. In the present study, the nitrogen partial pressure is 0.4 Pa, which is enough for the preferential formation of Si_3N_4 and W_2N phase. Thus, it is reasonable to consider that the addition of C into W–Si–N led to the formation of $W_2(C, N)$ solid solution.

In order to clarify the bonding state of W–Si–C–N coatings, XPS analysis was conducted, and the detailed spectra was shown in Fig. 4. The W4f spectrum of W–Si–N coating presents two peaks centered at 32.8 eV and 34.9 eV corresponding to the W4f7/2 and W4f5/2 of tungsten nitride [20,21], respectively. For W–Si–C–N coatings with different carbon content, two similar peaks appear nearly at the same position, indicating that the incorporation of carbon into W–Si–N coatings has not obvious effect on the W4f peaks. In the N1s spectra of W–Si–N coating, the N1s peak could be decomposed into two components centered at 397.3 eV and 397.7 eV, which is in good agreement with W—N and Si—N bonds in W_2N [20] and Si_3N_4 [22]. In the case of W–Si–C–N coatings, an additional peak appears at 398.2 eV, which is consistent with the value

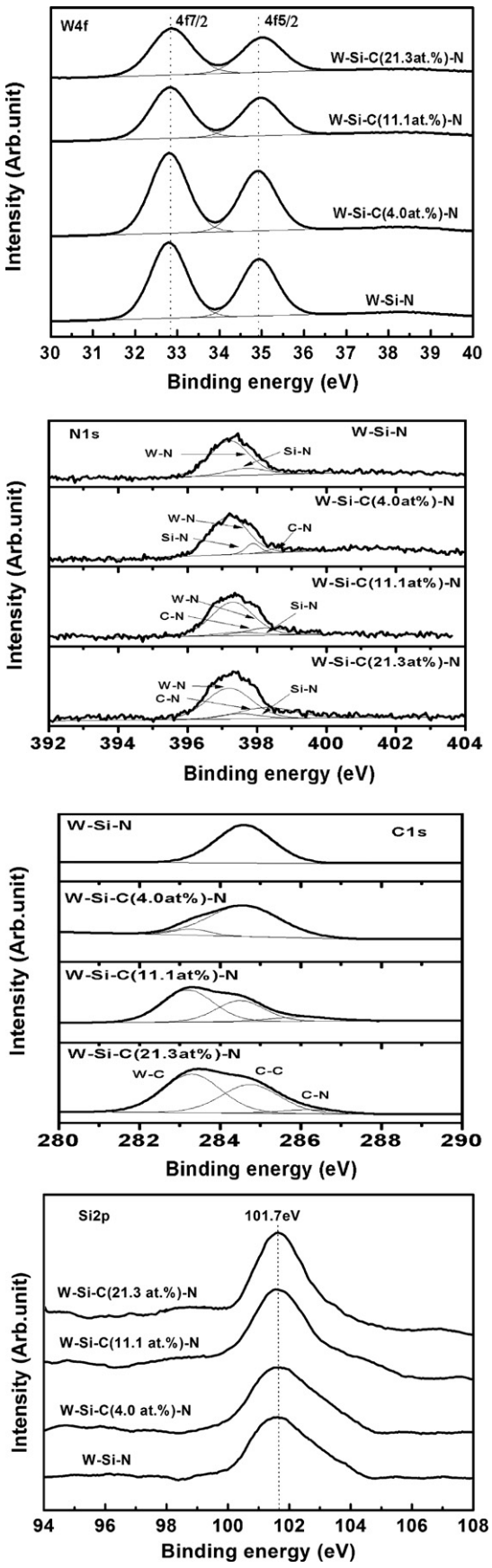

Fig. 4. XPS spectra of W4f, C1s, N1s, and Si2p of W–Si–C–N coatings.

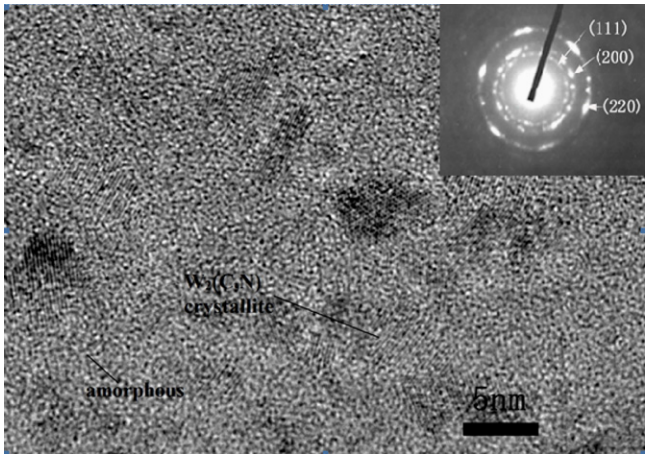

Fig. 5. High resolution TEM images and selected area electron diffraction (inset) of W–Si–C (11.1%)–N coating.

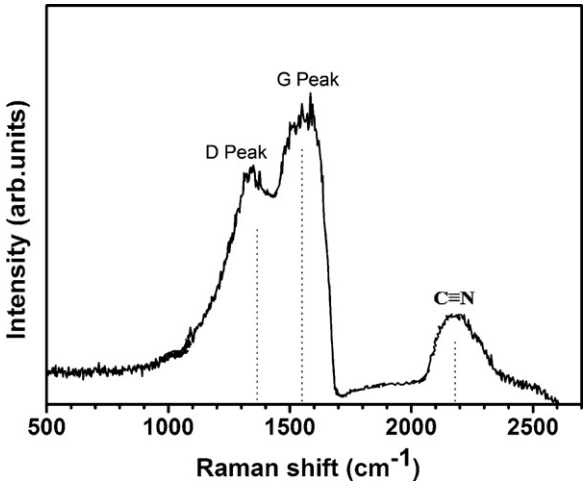

Fig. 6. Raman spectra of W–Si–C (11.1%)–N coating.

of N—C bonds (397.7–400.2) in carbon nitride films [23]. As the carbon content was increased, the intensity of peaks corresponding to W–N and Si–N decrease whereas intensity of C–N peak increases. The C1s spectra of W–Si–N coating show peaks at 284.7 eV that can be assigned to C—C bonds in amorphous carbon, suggesting the existence of carbon contamination. It is reported that the C1s peaks

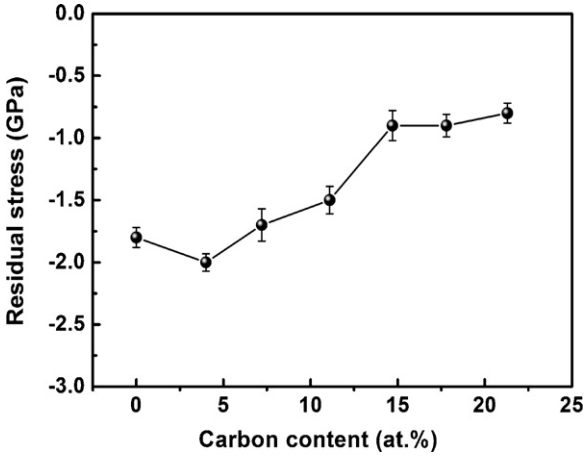

Fig. 7. Residual stress built in W–Si–C–N coatings.

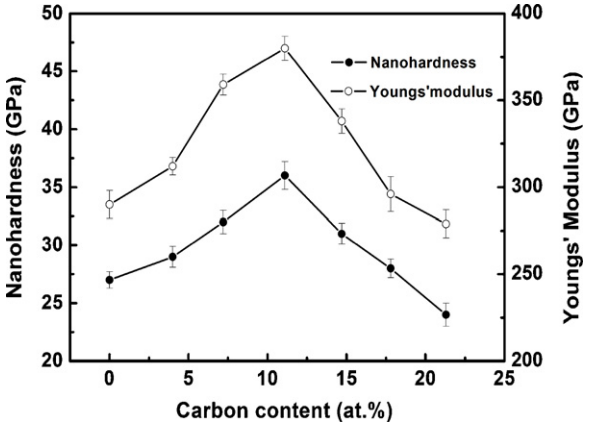

Fig. 8. Variation of hardness and Youngs' modulus of W–Si–C–N coatings with different carbon content.

of the coatings are difficult to assess because of adventitious carbon contamination of coating surface even after ion etching [24]. However, in the case of W–Si–C–N coatings, besides peak at 284.7 eV, two other peaks at 283.2 and 286.3 eV were observed which are close to the binding energy of W—C bond in WC_{1-x} and in consistent with the binding energy of C—N bonds in amorphous CNx, respectively. As for Si 2p spectra, for W–Si–N coating a peak centered at about 101.7 eV is observed, which is in good agreement with the binding energy of Si—N bond in Si_3N_4 [25]. As carbon was incorporated into W–Si–N coatings, the peak position did not change whereas the peak intensity varied slightly, indicating slight change of silicon content in W–Si–C–N coatings.

Fig. 8 exhibits the HRTEM micrograph and corresponding selected area electron diffraction (SAED) pattern (inset in Fig. 8) of W–Si–C–N coatings containing 11.1 at.% C. Small crystallite with a grain size of about several nanometers surrounded by amorphous zones can be seen, as indicated by solid line. The crystalline and amorphous phase can be distinguished from each other by lattice fringe contrast. The SAED is constituted of rings, exhibiting some spots originating from larger size of the crystallites in the coatings. From such a pattern the lattice constant can be calculated, which is in good accordance with the XRD results.

Raman spectroscopy was employed to characterize the carbon bonding of the coatings. Fig. 9 exhibits the Raman spectra of W–Si–C–N coatings containing 11.1 at.% C. As can be seen that two peaks centered at around 1360 and 1550 cm^{-1} are assigned to D and G peaks, respectively [26], which are related to stretch modes of sp^2 bonded C atoms [27]. In addition, a small and wide peak situated at around 2195 is assigned to C≡N bonds [28]. Raman analysis further confirms the existence of amorphous C and CNx phase. Based on XRD, XPS, HRTEM and Raman results, it can be concluded that W–Si–N coating consisted of crystalline W_2N phase and amorphous Si_3N_4 phase whereas W–Si–C–N coating consisted of crystalline $W_2(C, N)$ solid solution and amorphous Si_3N_4, CNx and amorphous carbon.

Fig. 5 presents the evolution of residual stress of W–Si–C–N coating with carbon contents. The measured residual stress here is a combination of both thermal stress and intrinsic stress. The thermal stress is originated from the difference in thermal expansion coefficient between silicon substrate and coatings, and from high substrate temperature during coating deposition. The intrinsic stress mainly refers to compressive stress, which are generated during film deposition using magnetron sputtering technique under low total sputtering pressure [29]. It can be seen that regardless of carbon content, all the coatings are in compressive stress state. For W–Si–N coating, the compressive stress is about −1.8 GPa. The addition of 4 at.% C into W–Si–N coating led to slight increase of

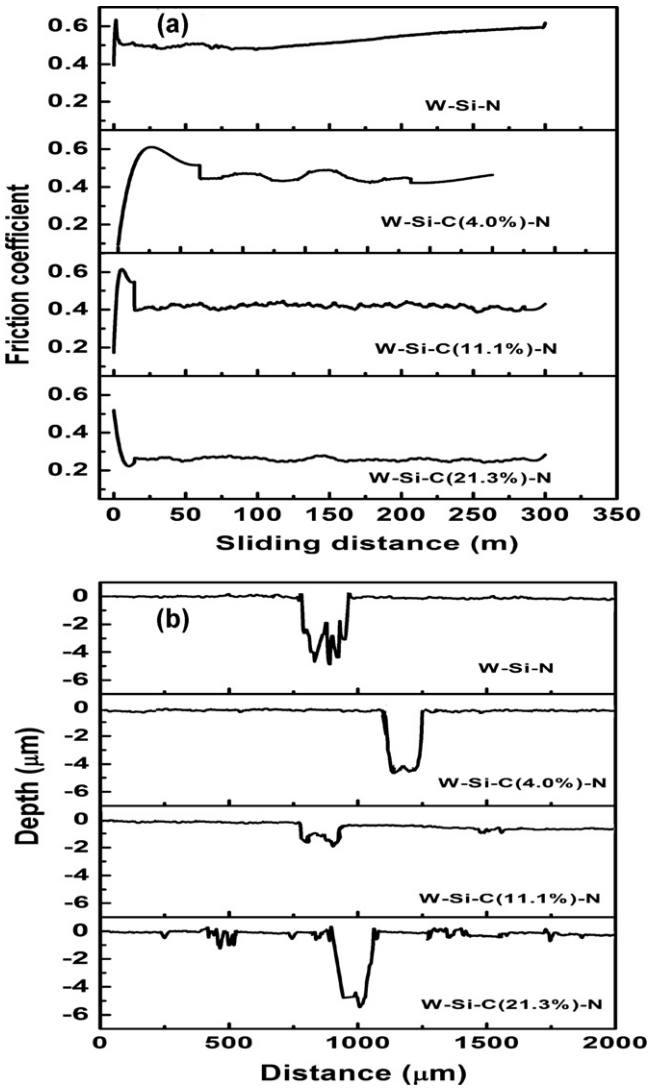

Fig. 9. (a) Friction coefficient of the films as a function of sliding distance, and (b) corresponding surface profiles of the wear tracks after friction test.

0.2 GPa in compressive stress, that is because of the incorporation of carbon atoms into W_2N crystal lattice. With further increase of carbon content, the compressive stress decrease gradually, which is due to formation of a large quantity of amorphous phase. Fu et al. [30] reported that residual stress can be partially released by amorphous phase due to their low density and disordered network.

3.2. Hardness and Youngs' modulus

The variation of hardness and Young's modulus of W–Si–C–N coatings with carbon content is shown in Fig. 6. The hardness and Youngs' modulus of W–Si–N coating is 27 GPa and 290 GPa, respectively. With carbon content increasing from 0 at.% to 21.3 at.% the hardness and Youngs' modulus first increased gradually and then decreased, after passing the maximum value of 36 GPa and 380 GPa, respectively, at 11.1 at.% C. As for hardness enhancement of hard coating, there exist several different mechanisms mainly including Hall–Petch effect, solid solution hardening, precipitation hardening [31–35]. In addition, it is well known that compressive stress built into coatings can play a positive role in hardness enhancement. In our case, at least four factors contribute to hardness enhancement. Firstly, the nanocomposite structure consisting of $W_2(C, N)$ nanocrystalline and amorphous Si_3N_4/CNx/C are beneficial for hardness enhancement. Secondly, carbon atoms dissolving into W_2N crystal lattice act as solid solution hardening. Thirdly, as the carbon concentration is below 11.1 at.%, the hardness of coatings increase with crystallite size decreasing, which indicated that Hall–Petch effect works. However, as the carbon concentration is beyond 11.1 at.%, Hall–Petch law does not work, which was confirmed by the decreasing of hardness with crystallite size decreasing. The last reason for hardness evolution is the change of residual stress. As seen, there is optimum carbon content (11.1 at.%) in W–Si–C–N coatings at which the hardness and Young's modulus reach maximum value of 36 GPa and 382 GPa, respectively. Vepřek et al. reported that the hardness of nanocomposite Ti–Si–N coatings is sensitive to silicon content in coatings, and reach maximum value as the thickness of amorphous Si_3N_4 is about 1 monolayer, corresponding to approximately 8 at.% Si in coatings [36,37]. This phenomenon is also valid for the relationship between carbon content and hardness of the W–Si–C–N coating in our case when the silicon concentration is kept unchanged. The decrease in hardness of W–Si–C–N coating with carbon content increasing could be explained from two aspects: First, decrease in compressive stress. Second, carbon content in coatings is in excess of the optimum value.

3.3. Tribological behaviour

Fig. 7 shows the friction coefficient of the films against sliding distance and the corresponding wear tracks on the films after friction test. On the whole, the W–Si–C–N coatings show a lower friction coefficient compared with W–Si–N films. Friction coefficient decreased from 0.5 for W–Si–N to 0.26 for W–Si–C (21.6 at.%)–N with increasing carbon content. The decrease of friction coefficient with carbon addition is mainly due to the formation of amorphous carbon, which could play lubricant effect as self-lubricating materials, as already reported by Abraham [38]. Correspondingly, the wear tracks of W–Si–C–N coatings became shallower and narrower as the carbon content increase from 0 at.% to 11.1 at.% and then get much deeper and wider for coating containing 21.3 at.% C (as observed in Fig. 7b), indicating the wear resistance of W–Si–C–N coatings increase at first and then decrease with increasing carbon content. According to Archards wear equation:

$$\frac{V}{L} = K\frac{W}{H} \quad (1)$$

where V, L, K, W, H represent the wear volume of materials removed, the sliding distance, Archards wear coefficient, normal load and coating hardness, respectively. Here, L and W are kept constant at 300 m and 2 N, respectively. The wear volumes are reverse ratio to hardness of coatings. Thus, the volume of wear track of W–C–Si–N coatings shows nearly opposite variation trend to that of hardness with the increase of carbon content. It is well known that wear results from friction. Thus, wear resistance of coatings closely related to friction coefficient and hardness of coatings. In our case, the initial enhanced wear resistance can be ascribed to the decrease of friction coefficient and improvement in hardness whereas the reduced wear resistance is mainly due to the sharp decrease in hardness.

4. Conclusions

W–Si–C–N coatings were deposited onto silicon wafer substrates using magnetron sputtering technique. The influence of carbon content on the phase composition, microstructure, chemical bonding state, residual stress, friction coefficient, hardness and Youngs' modulus were investigated in details. The main results can be concluded as follows:

(1) W–Si–C–N coatings possess nanocomposite microstructure consisting of W–C–N nano-crystallites and amorphous phase of Si_3N_4/CNx/C.
(2) Residual stress built in coatings are in compressive state, and increased from 1.8 GPa to 2.0 GPa as carbon content increased from 0 at.% to 4 at.%, then decreased with further increase of carbon content.
(3) Hardness and Youngs' modulus of W–Si–C–N coatings first increased and then decreased, after passing the maximum value of 36 GPa and 382 GPa, respectively, for coatings containing 11.1 at.% C, because of nanocomposite structure, reduced crystallite size, and high compressive stress.
(4) Friction coefficient of W–Si–C–N coatings decreased greatly from 0.5 for W–Si–N to 0.26 for W–Si–C (21.6 at.%)–N due to the formation of amorphous carbon as self-lubricating materials. Correspondingly, the wear volume of wear debris of W–C–Si–N coatings shows nearly opposite change trend to that of hardness with the increase of carbon content.

Acknowledgments

This work has been subsidized by the National Natural Science Foundation of China (Grant No. 51101152).

References

[1] S. Vepřek, S. Reiprich, S.Z. Li, Applied Physics Letters 66 (1995) 2640.
[2] J.S. Colligon, V. Vishnyakov, R. Valizadeh, S.E. Donnelly, S. Kumashiro, Thin Solid Films 485 (2005) 148.
[3] K.H. Kim, S.-R. Choi, S.-Y. Yoon, Surface and Coatings Technology 298 (2002) 243.
[4] H.Y. Zhao, Q.L. Fan, L.X. Song, T. Zhang, E.W. Shi, X.F. Hu, Applied Surface Science 252 (2006) 3065.
[5] S. Vepřek, M.G.J. Veprek-Heijman, P. Karvankova, J. Prochazka, Thin Solid Films 476 (2005) 1.
[6] A. Niederhofer, P. Nesladek, H.-D. Männling, Surface and Coatings Technology 120–121 (1999) 173.
[7] S. Vepřek, M. Haussmann, S. Reiprich, S.Z. Li, J. Dian, Surface and Coatings Technology 86–87 (1996) 394.
[8] S. Ma, J. Procházka, P. Karvánková, Q. Ma, X. Niu, X. Wang, D. Ma, K. Xu, S. Vepřek, Surface and Coatings Technology 194 (2005) 143.
[9] I.-W. Park, S.R. Choi, J.H. Suh, C.-G. Park, K.H. Kim, Thin Solid Films 447–448 (2004) 443.
[10] O.-N. Park, J.H. Park, S.-Y. Yoon, M.-H. Lee, K.H. Kim, Surface and Coatings Technology 179 (2004) 83.
[11] J.-H. Jeon, S.R. Choi, W.S. Chung, K.H. Kim, Surface and Coatings Technology 188–189 (2004) 415.
[12] T. Fu, Z.F. Zhou, K.Y. Li, Y.G. Shen, Materials Letters 59 (2005) 618.
[13] C. Louro, A. Cavaleiro, Surface and Coatings Technology 116–119 (1999) 74.
[14] A. Czyzniewski, Thin Solid Films 433 (2003) 180.
[15] J.F. Yang, Z.G. Yuan, G.G. Zhang, X.P. Wang, Q.F. Fang, Materials Research Bulletin 44 (2009) 1948.
[16] D.Y. Ma, S.L. Ma, H.S. Dong, K.W. Xu, T. Bell, Thin Solid Films 496 (2006) 438.
[17] S.L. Ma, D.Y. Ma, Y. Guo, B. Xu, G.Z. Wu, K.W. Xu, P.K. Chu, Acta Materialia 55 (2007) 6350.
[18] Y. Guo, S.L. Ma, K.W. Xu, Surface and Coatings Technology 201 (2007) 5240.
[19] H.J. Goldschmidt, Interstitial Alloys, Butterworth & Co., London, 1967.
[20] Y.G. Shen, Y.W. Mai, D.R. McKenzie, Q.C. Zhang, W.D. McFall, W.E. McBride, Journal of Applied Physics 88 (2000) 1380.
[21] H.T. Chiu, S.H. Chuang, Journal of Materials Research 8 (1993) 1353.
[22] S. Vepřek, Journal of Vacuum Science and Technology A 17 (1999) 2401.
[23] D.Y. Lee, Y.H. Kim, I.K. Kim, H.K. Baik, Thin Solid Films 355–356 (1999) 239.
[24] C.D. Wagner, L.E. Davis, M.V. Zeller, J.A. Taylor, R.H. Raymond, L.H. Gale, Surface and Interface Analysis 3 (1981) 211.
[25] J.L. Bischoff, F. Lutz, D. Bolmont, L. Kubler, Surface Science 251–252 (1991) 170.
[26] A.C. Ferrari, J. Robertson, Physical Review B 61 (2000) 14095.
[27] F.X. Liu, K.L. Yao, Z.L. Liu, Applied Surface Science 253 (2007) 6957.
[28] J. Robertson, Diamond and Related Materials 13 (2004) 1558.
[29] Y.G. Shen, Materials Science and Engineering A 359 (2003) 158.
[30] T. Fu, Z.F. Zhou, K.Y. Li, Y.G. Shen, Surface and Coatings Technology 200 (2005) 2525.
[31] E.O. Hall, Proceedings of the Physical Society. Section B 64 (1951) 747.
[32] N.J. Petch, The Journal of the Iron and Steel Institute 174 (1953) 25.
[33] S.J. Heo, K.H. Kim, M.C. Kang, J.H. Suh, C.-G. Park, Surface and Coatings Technology 201 (2006) 4180.
[34] Z.J. Liu, P.W. Shum, Y.G. Shen, Thin Solid Films 468 (2004) 161.
[35] Y.G. Shen, Z.J. Liu, N. Jiang, H.S. Zhang, K.H. Chan, Z.K. Xu, Journal of Materials Research 19 (2004) 523.
[36] S. Vepřek, R.F. Zhang, M.G.J. Veprek-Heijman, S.H. Sheng, A.S. Argon, Surface and Coatings Technology 204 (2010) 1898.
[37] S. Vepřek, S. Reiprich, Thin Solid Films 268 (1995) 64.
[38] S. Abraham, E.Y. Choi, N. Kang, K.H. Kim, Surface and Coatings Technology 202 (2007) 915.